Enhanced Opto–Electronic Properties of Bi:CuO/n-Si Heterojunctions for Photodetector Applications

G. Sutcu[a], S. Yigit Gezgin[b], S. Baturay[c,*] and H.S. Kilic[b,d,e]

[a]*Department of Physics, Institute of Natural Sciences, Dicle University, 21280 Diyarbakir, Turkey*
[b]*Department of Physics, Faculty of Science, University of Selcuk, 42031 Selcuklu, Konya, Turkey*
[c]*Department of Physics, Faculty of Science, Dicle University, 21280 Diyarbakir, Turkey*
[d]*Directorate of High Technology Research and Application Center, University of Selcuk, 42031 Selcuklu, Konya, Turkey*
[e]*Directorate of Laser Induced Proton Therapy Application and Research Center, University of Selcuk, 42031 Konya, Turkey*

An effective photodetector based on a family of p-type semiconductors with unique properties is still required by current trends in optoelectronics. The purpose of this study is to enhance the performance of p-type copper oxide films by doping them with bismuth. The pure copper oxide films were successfully fabricated with 1, 2, and 3 wt% of Bi by the spin coating method in an air atmosphere. Advanced techniques were used to describe the fabricated non-doped and Bi-doped CuO films to understand their structural, topological, and optical characteristics. X-ray diffraction patterns of non-doped and Bi-doped CuO films have demonstrated that they have polycrystalline structures, with a preference for growth in both (-111) and (200) orientations. Copper oxide film with 2% Bi doping exhibited the most uniform particle size distribution compared to others. While 3% Bi-doped CuO thin film exhibits the highest photon absorption, 2% Bi-doped CuO thin film transmits more photons. The direct band gaps of the non-doped and Bi-doped CuO samples were found between 1.77 and 1.94 eV. Copper oxide thin film with 2% Bi has the lowest refractive index. While the 2% Bi-doped CuO heterojunction photodetector shows the highest photosensitivity, responsivity, and detectivity, its rise and time are the lowest. Since 2% Bi-doped CuO film has a good crystal structure, large crystalline size, low particle boundary numbers, and a more homogeneous particle size distribution, the number of traps and defects in this thin film is low, and the recombination of charge carriers is limited. Thus, this thin-film-based heterojunction exhibited the best photodetector property, and the results of this work give a way to create effective photodetectors and adjust their performance over a broad range.

topics: Bi-doped CuO, spin coating, photodetector, rise time

1. Introduction

Great attention is given to nanomaterials since they are so highly demanded in the semiconductor industry. Photodetectors (PDs) made from nano-materials are used in a variety of energy-related applications and commercial applications, which makes them an important component of modern opto–electronic (OE) devices [1, 2]. Even though Ge/Si-based PDs have already become commercially viable, the manufacturing processes are extremely expensive, the opto–electrical properties are unstable, and the driving voltages are high. There is some need for low-cost, high-speed photo-detecting materials with stable OE properties for photodetection purposes [3–5].

Transparent semiconducting oxide (TSO) materials such as copper oxide have been extensively investigated for diverse applications. The copper oxide crystallizes in two forms: cuprous or cuprite oxide (Cu_2O) and cupric or tenorite oxide (CuO). CuO in a monoclinic state has a direct energy band of around 1.2–2.0 eV [6, 7], whereas Cu_2O in a cubic state has a direct energy band gap of about 2.1–2.7 eV [8, 9]. Copper oxides are a unique family of p-type semiconductors that display a high optical absorption coefficient in both near-infrared (NIR) and visible ranges because of their energy band value [10]. CuO with an energy band value of 1.5 eV can achieve a maximum heterojunction solar cell efficiency value of nearly 30%, significantly greater than the highest limit of 20% for Cu_2O with an energy band of ~ 2 eV [11, 12]. CuO thin film, a p-type semiconductor with unique properties, has inspired researchers, and the widespread availability of CuO and its low cost make it more popular for use. The thermal stability of CuO and its structural and chemical properties

allow it to be used in electrochemical supercapacitors, solar cell applications, CO_2 sensors, and other devices [13–17]. Intriguingly, both the physical and chemical properties of CuO may depend on many parameters, including deposition technique, topology, temperature, or doping of the parental nanomaterial [18–20].

It is also becoming increasingly important to develop Bi^{3+}-based structures as semiconductors. There are many oxides based on Bi^{3+} that conduct in semiconductors, with exclusive features resulting from aliovalent doping or native Bi vacancies [21]. The involvement of Bi^{3+} $6s^2$ lone pair states at the valence band (VB) could also provide a dispersive valence band maximum (VBM) for hole transportation, resulting in high p-type mobility, as indicated in the cases of $BiVO_4$ and p-type BiOI [22]. Additionally, heavy metal cations (Bi^{3+}) doped transition metal oxides (TMO) possessing both delocalized and isotropic $6s$ orbitals and hybridizing with O $2p$ orbitals to create pseudoclosed ns^2 lone pair orbitals in VBM are predicted to indicate high p-type hole mobility because of reduced VBM localization [23]. In addition, in recent years, $CuBi_2O_4$ semiconductors with a direct energy band between $\sim$ 1.4 and 1.8 eV have also been recognized as potential materials for photoelectrochemical solar cells, photocatalysis, and solar fuels [24–26]. To enable the use of characteristics of CuO in different applications, various deposition techniques have been created to obtain different topologies of CuO nanostructures [27–29]. Using the spin coating deposition technique, Prabhu et al. [30] have reported a heterojunction diode with p-CuO/n-ZnO with efficient UV absorption by the semiconducting layer. The electrical characterization of green-produced p-CuO/n-ZnO heterojunction diode was analyzed by Annathurai et al. [31]. In their paper, Zhang et al. [32] noted the detectivity of 3.27×10^8 Jones for the flexible light detector made of p-CuO/n-MoS$_2$ heterojunction diode with enhanced photocurrent and detection sensitivity. Hong et al. [33] have improved a CuO/Si nanowire-based broadband photodetector via a solution synthesis technique and analyzed it through the test at various wavelengths, and they have indicated that CuO-based nano photodetector exhibits ultrafast reaction rise and recovery periods of $\sim$ 60 and 80 s, respectively. Fu et al. [34] have deposited a ZnO/CuO photodetector by hydrothermal technique and noted that sensitivity and responsivity had values of 120 and 0.272 mA/W, respectively. Various methods, including ultrasonic spray pyrolysis (USP) method, pulsed laser deposition (PLD), chemical vapor deposition (CVD), and reactive ion beam sputter deposition (IBSD) method, have been explored to create a CuO and associated photosensitive/photo-absorber layers [35–38]. The aforementioned techniques have drawbacks, such as the need for vacuum conditions and layer thickness control.

Thin-film coating of desired designed nanostructures of high performance is possible with solution-processing film preparation without destroying their topology. Using this technique, the photosensitive layers can be created affordably, effectively, and simply [39]. Additionally, the solution-processed film-making technique improves the light absorption efficiency, and charge carriers under light conditions are transported by photo-generated recombination of electron–hole pairs of the large surface of the core-shell structure free from any loss [40].

The studies mentioned above demonstrate that the characteristics of non-doped CuO have been significantly enhanced or changed when prepared by various deposition techniques, synthesis, and layers. The doping of metal ions has an important impact on the structural, topological, and optical characteristics of CuO films. However, few experimental studies on Bi-doped CuO thin film have been reported in the literature. Thus, for a better understanding of Bi dopant effect on the physical characteristic of CuO film, it is necessary to perform more experimental studies. For this reason, we have focused on modifying the physical properties of CuO samples related to the Bi doping ratio using a simple and low-cost technique. We have successfully fabricated non-doped and Bi-doped CuO samples by spin technique on soda lime glass (SLG) substrates using ethanol solvent and 1:10 triethanolamine. Physical properties, including crystal parameters, surface properties, absorbance, and energy band gap, have been investigated and analyzed by X-ray diffraction (XRD) systems, atomic force microscopy (AFM), and UV-Vis measurement systems in order to gain more knowledge about Bi:CuO semiconductor, which needs further widespread work on the physical parameters of the film. Using J–V properties, the n-Si/Bi:CuO heterojunction diode was examined in both dark and light conditions. The important photodiode parameters have been calculated and explained, including ideality factor, barrier height (Φ_b), serial resistance, photosensitivity, responsivity, detectivity, and rise and fall times of the photodetectors.

2. Experimental procedures

2.1. Thin film synthesis

In the present work, 40 mL of ethanol was used to dissolve 0.1 M copper (II) acetate monohydrate (($CH_3COO)_2Cu \bullet H_2O$), 0.2 mL of triethanolamine was added as a stabilizer at room temperature, and 20 mL of ethanol was used to dissolve bismuth (III) chloride ($BiCl_3$) (0.01 M). In order to obtain a clear blue solution, Cu/Bi solutions were slowly mixed and stirred at room temperature to obtain the desired molar ratio. Doping concentrations of 1, 2, and 3% were used to prepare non-doped and Bi-doped copper (II) acetate monohydrate solutions.
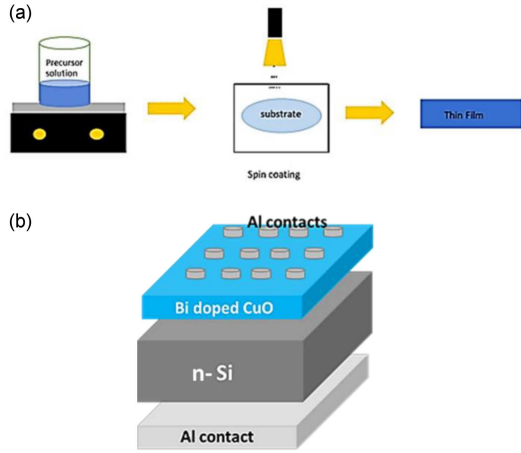
Fig. 1. Schematic diagram of Bi:CuO film deposition processes.

To remove organic contaminants, the SLG substrates were first ultrasonically rinsed with acetone and cleaned in ethanol for 5 min each before the spin coating process. After drying with an air gun, the SLG substrates were baked at 120°C for 5 min to eliminate any remaining moisture. Then, to obtain Bi:CuO/n-Si diode, Si-wafers were boiled in trichloroethylene for around 5 min at 90°C and then stirred for 5 min in deionized water twice each and in ethanol absolute to get rid of any organic and chemical residues in an ultrasonic bath. Hydrofluoric acid (HF)–distilled water (H_2O) solution (1:10) was used to etch Si-wafers, which were washed twice for 25 s with distilled water to remove the native oxide contaminations before installing them in the vacuum chamber to obtain Bi:CuO/n-Si diode. After evaporating a 200 nm thick aluminum contact layer on the unpolished side of the Si-wafer, the back contacts were thermally annealed at 420°C for 180 s under N_2. The precursor solutions were spin-coated at 1500 rpm for 60 s and dried on a hot plate at 220°C for 8 min in air conditions to achieve the best results; the schematic of this mechanism is given in Fig. 1. To produce the non-doped, Bi:CuO (1%), Bi:CuO (2%), and Bi:CuO (3%) thin films, spin coating and drying were performed ten times for SLG substrates and three times for Si-wafers. Finally, Al front contacts were evaporated onto the Bi:CuO thin films using a shadow mask, and all of the obtained samples were annealed at 480°C for 60 min.

2.2. Structural and optical characterization

Rigaku Ultima III X-ray diffractometer (XRD) was used to analyze the purity, phase, and crystallization of the annealed Bi:CuO (0%), Bi:CuO (1%), Bi:CuO (2%), and Bi:CuO (3%) thin films using monochromatic Cu K_α radiation with an operating voltage (V) and current (I) of 40 kV

and 30 mA, respectively. The crystallite size (D), inter-planar spacing (d), micro-strain (ε), and dislocation density (δ) of Bi-doped CuO films were analyzed using the diffraction data obtained from XRD. Topology of Bi:CuO (0%), Bi:CuO (1%), Bi:CuO (2%), and Bi:CuO (3%) thin films on SLG substrate was studied by atomic force microscopy (XEI software, Park Systems). A UV-3600 spectrophotometer (Shimadzu, Tokyo, Japan) ran over a spectral range of 300–1100 nm, and absorbance spectra were recorded. Photodetecting properties of all obtained thin films were carefully measured by a Keithley SourceMeter 2450 using a 532 nm laser wavelength.

3. Discussion

3.1. XRD properties

XRD patterns of non-doped and Bi-doped CuO films are given in Fig. 2. The 2θ angle peaks are at approximately 32.8°, 35.9°, 39.0°, 53.8°, and 68.2°, and d_{hkl} of approximately 2.73 Å, 2.50 Å, 2.30 Å, 1.70 Å, and 1.37 Å were indexed to the non-doped CuO phase (JCPDS 05–6661) reflections from (110), (−111), (200), (020), and (220) planes, respectively. It was reported and can be concluded based on XRD patterns that all samples indicate a typical tenorite CuO structure [41]. Similar observations regarding XRD data were reported by Akgul et al. in [7]. Relatively stronger peak intensities indicate a preferential orientation (200) for all samples, and the intensity of prominent peaks increased with Bi doping ratios compared to non-doped CuO. The results may be explained by the type of bond formed between atoms contained in thin films. Johan et al. [41] have demonstrated similar results, and they have indicated that CuO thin films with a thickness of $\sim$ 450 nm had a preferential orientation in (111) and (200) directions. Peak intensity and FWHM (full width at half maximum) values used to calculate the crystallite size change with increasing Bi concentrations. The peak intensity significantly increased with the increase in Bi concentration in thin film during CuO deposition due to a larger ionic radius of Bi^{3+} (1.03 Å) than the ionic radius of Cu^{2+} (0.74 Å). Bi ions can readily replace Cu sites due to their higher solubility limit. Based on these findings (peak intensity, peak broadening, and shift on the peak), it is evident that Bi^{3+} ions were effectively integrated into the CuO structure.

As shown in Table I, XRD patterns have been used to calculate crystallite size (in nm units), dislocations (in m^{-2}), orientation (hkl), inter-planar spacing, and micro-strain (ε) values. The crystallite size (D) of CuO samples is carefully calculated for two main peaks, (−111) and (200), using Debye–Scherrer's formula [42]

$$D = \frac{k\lambda}{\beta \cos(\theta)}, \qquad (1)$$

FWHM, crystal size, and orientation of the non-doped and Bi-doped CuO thin films obtained by XRD data.

Sample	FWHM	2θ [degree]	D [nm]	d-spacing [Å] (calculated)	d-spacing [Å] (standart)	δ ($\times 10^{15}$) [m^{-2}]	ε (8×10^{-4})	hkl
Non-doped	0.19	32.82	42.69	2.73	2.729	0.55	0.29	110
	0.33	35.87	24.97	2.50	2.503	1.60	0.45	−111
	0.47	39.02	22.52	2.30	2.318	1.97	0.16	200
	0.42	53.77	20.79	1.70	1.705	2.31	0.37	020
	0.32	68.26	29.68	1.37	1.374	1.14	0.21	220
1% Bi:CuO	0.32	35.90	26.07	2.50	2.502	1.14	0.43	−111
	0.52	39.08	17.10	2.30	2.305	3.42	0.21	200
2% Bi:CuO	0.40	35.88	20.82	2.50	2.503	2.31	0.54	−111
	0.38	39.01	23.80	2.31	2.309	1.77	0.15	200
	0.20	53.71	45.43	1.71	1.707	0.49	0.17	020
3% Bi:CuO	0.26	35.87	32.41	2.50	2.503	0.95	0.34	−111
	0.35	38.97	16.04	2.31	2.311	3.88	0.23	200

where k is referred to as the crystallite-shape (~ 0.89), λ is the wavelength of X-ray diffractometer, β and θ are FWHM value and Bragg's diffraction angle of XRD peaks using monochromatic Cu K_α radiation, respectively. The calculated crystallite parameters for the obtained non-doped and Bi-doped CuO samples are given in Table I.

As a consequence of molecular concentration at the crystal surface of films, D value for the (-111) peak increased with both 1% and 3% Bi-doping compared to non-doped CuO, while the maximum D value for the (200) peak was achieved by 2% Bi-doped CuO film. Qutbi et al. [43] have indicated that crystallite size increased with Bi doping because of the combined effect of the change in Cu incorporation and a change in the rate of growth. Bragg's equation is used to calculate the inter-planar spacing values for films

$$2d\sin(\theta) = n\lambda. \tag{2}$$

The order of diffraction is given by n. The calculated d values of non-doped and Bi-doped CuO samples for (-111) and (200) are around 2.50 Å and 2.30 Å, respectively. To calculate the density of defects in the crystal structure, the dislocation density value (δ) of films is calculated by [44]

$$\delta = \frac{1}{D^2}. \tag{3}$$

The micro-strain (ε) values of obtained thin films are calculated using the following [45]

$$\varepsilon = \frac{1}{\sin(\theta)}\left[\left(\frac{\lambda}{D}\right) - \beta\cos(\theta)\right]. \tag{4}$$

The calculated crystallite size (D) for preferential orientation increases from 22.52 to 23.80 nm compared to non-doped CuO, and micro-strain and dislocation values, on the contrary, decrease from 0.16×10^{-4} to 0.15×10^{-4} and from 1.97×10^{15} to 1.77×10^{15} lines/m^2 for 2% Bi-doped CuO film, respectively. The calculated crystallite size with
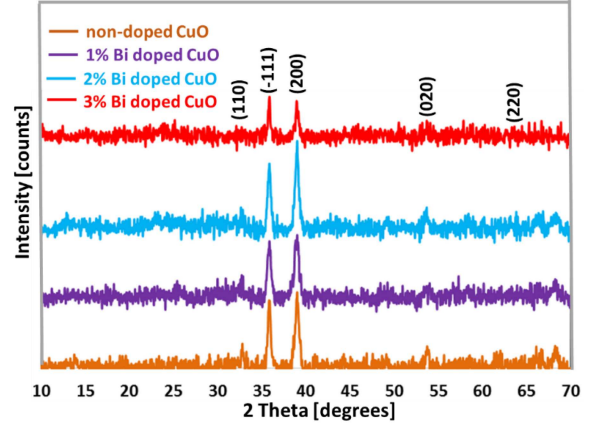

Fig. 2. XRD pattern of the 0%, 1%, 2%, and 3% Bi-doped CuO films.

increasing Bi doping ratio in CuO film for orientation of (-111) increases from 24.97 to 32.41 nm compared to non-doped CuO. The calculated crystallite size of 2% Bi-doped CuO film for main orientation as compared to the other samples indicates a higher crystallite value owing to a smaller FWHM value and the expansion of structural parameters due to the presence of Bi dopants in the solution.

The highest crystallite size and lowest micro-strain values achieved by doping 2% Bi with CuO for the main peak are expected to be used in photo-sensing devices. It was seen that Bi concentrations caused a change in the dislocation density value of the films' preferred orientation, which may be explained by the occurrence of micro-strain in Bi:CuO samples. Micro-strains of the (-111) and (200) planes significantly change with Bi content. Consequently, it was concluded that micro-strain differentials are the main reason for the change in value. Reduced micro-strain implies reduced lattice
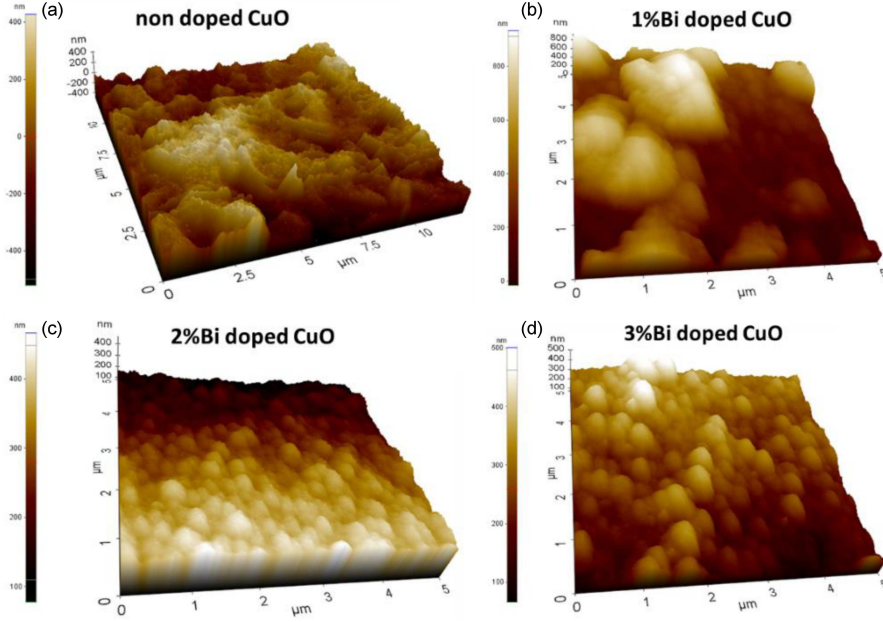
Fig. 3.   AFM images of (a) the non-doped, (b) 1%, (c) 2%, and (d) 3% Bi-doped CuO thin films.

imperfections and the creation of high-quality samples. It was demonstrated by Mageshwari and Sathyamoorthy [6] that the change in crystallite size from 7 to 11 nm resulted in a decrease in both micro-strain and dislocation density.

3.2. Morphological properties of the non-doped and Bi-doped CuO thin films

As seen in the AFM image given in Fig. 3, the non-doped CuO thin film has an irregular particle structure. When CuO was doped with 1% Bi, the size of particles forming the thin film increased, but the particle size distribution was not homogeneous. With 2% Bi doping, more uniform nucleation occurs in the particles, and the size distribution of the particles becomes more and more uniform. With 3% Bi doping, on the other hand, since the doping rate is high, it causes a partial increase in the height of the particles. The roughness values of 0%, 1%, 2%, and 3% Bi-doped CuO samples are found to be 0.14, 6.43, 6.85, and 9.34 nm, respectively.

3.3. Optical properties of non-doped and Bi-doped CuO/Si thin films

According to the transmission spectra in Fig. 4a, 1% and 2% Bi-doped CuO thin films exhibited very similar optical properties. These thin films transmit high photons in the NIR region of the solar spectrum, while the non-doped CuO thin film shows the lowest photon transmission in this region. Therefore, the Bi element increased the photon transmission of CuO thin film in the NIR region.
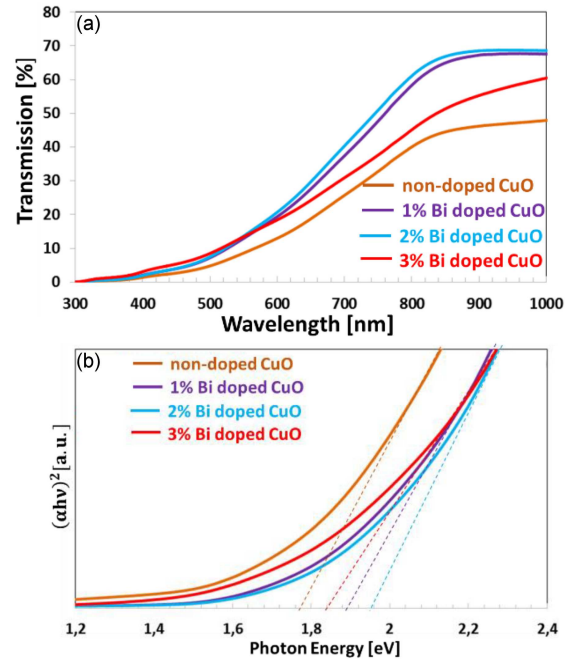

Fig. 4.   (a) Transmission and (b) the Tauc plot of the non-doped and Bi-doped CuO thin films.

The direct band gap of a sample can be calculated by the Tauc equation [46]

$$\alpha h\nu = A\left(h\nu - E_g\right)^{1/2}, \tag{5}$$

where $h\nu$ is photon energy, and A is an energy-independent constant. Herve and Vandamme [47] used (5) as the definition for photon energy. The energy band gap was obtained by straight line of $(\alpha h\nu)^2$ vs photon energy $(h\nu)$ in Tauc plot

TABLE II

The energy band, high frequency dielectric constant (ε_∞), and refractive index (n) of the Bi:CuO samples.

Samples	E_g [eV]	Moss relation 6		Herve & Vandamme (7)		Ravindra (8)	
		n	ε_∞	n	ε_∞	n	ε_∞
Non-doped CuO	1.77	2.79	7.81	2.81	7.91	2.65	7.05
1% Bi-doped CuO	1.89	2.74	7.55	2.75	7.60	2.55	6.52
2% Bi-doped CuO	1.94	2.73	7.46	2.73	7.48	2.51	6.30
3% Bi-doped CuO	1.84	2.76	7.66	2.78	7.73	2.59	6.73

in Fig. 4b. According to Tauc plot in Fig. 4b, the direct band gaps of Bi:CuO (0%), Bi:CuO (1%), Bi:CuO (2%) and Bi:CuO (3%) samples were found to be between 1.77 and 1.94 eV. The calculated direct band gaps of these thin films changed as photon transmission changed (or photo absorption increased) towards the longer wavelength region of the solar spectrum. Furthermore, due to Bi interstitial defects, the band gap of Bi:CuO (3%) sample is lower compared to other Bi-doped CuO samples [48].

The refractive index (n) of a semiconductor plays a key role in determining the capacity of a photodetector. The Moss relation [46]

$$E_g n^4 = k \tag{6}$$

is used to calculate the n value based on the band gap value. In (6), k is an energy-independent constant (~ 108 eV). Also, the relation between refractive index and direct energy band, used by Herve and Vandamme [47], is defined as

$$n = \sqrt{1 + \left(\frac{A}{E_g + B}\right)^2}, \tag{7}$$

where the corresponding values of A (13.6 eV) and B (3.4 eV) are constants. In addition to the Moss and Herve and Vandamme relations ((6) and (7)), an interesting equation between E_g and n was stated by Ravindra et al. [49] as

$$n = 4.16 - 0.85 E_g. \tag{8}$$

The refractive index values of the non-doped and Bi-doped CuO samples are obtained by using (6), (7), and (8), and they are also indicated in Table II. The Herve and Vandamme (7), Moss (6), and Ravindra (8) relations state that while thin films' direct energy band gaps are increased, thin film's refractive index value is slightly decreased. In particular, the high n value of Bi:CuO (0%) thin film can be explained by attributing it to the high photon absorption, extinction coefficient, and optical conductivity. Regarding the calculated results of the dielectric index and refractive index by Herve and Vandamme (7) and Moss (6), they all are close to each other, while the calculation results by Ravindra (8) show a slight difference.

The electric field created between charges in semiconductor thin films expressed by the dielectric coefficient (ε_∞) is a key component for the determination of the accumulation of charges, fast charge transfer, and charge separation in the depletion region in a heterojunction photodetector. The high-frequency ε_∞ values were determined using

$$\varepsilon_\infty = n^2. \tag{9}$$

The light lost due to scattering and absorption is determined by the calculation of extinction coefficient (k). The value of k is calculated by [50]

$$k = \frac{\alpha \lambda}{4\pi}, \tag{10}$$

where α is the absorption coefficient. Then, the equation $\alpha = 2.303(A/T)$, where A and T are the absorbance and thickness values of the thin film, respectively, is used to calculate the absorption coefficient of thin films. Obtained film thickness for non-doped and 1%, 2%, and 3% Bi:CuO films were found to be about 458, 486, 457, and 453 nm, respectively. The non-doped CuO sample has the highest k value in UV to NIR wavelength regions. In NIR region, 3% Bi-doped CuO sample has a higher k value than 1% and 2% Bi-doped CuO thin films. However, this sample has a lower k value between 300 and 570 nm, compared to the other thin films. Skin depth (δ_{SD}) describes the distance traveled by the light penetrating the samples' thickness. The skin depth of the samples is determined using [51]

$$\delta_{SD} = \frac{\lambda}{2\pi k}. \tag{11}$$

CuO samples with 1% and 2% Bi doping have higher δ_{SD} values at low photon energy. Here, the values of n are calculated from the Moss relation (6). In this region, these thin films are likely to diffuse deeply, since their absorption coefficient is lower. However, the magnitude of α value of the non-doped CuO sample in these ranges caused the skin depth to be low.

The optical conductivity (σ_{opt}) of all samples is determined using [50]

$$\sigma_{opt} = \frac{\alpha n c}{4\pi}, \tag{12}$$

where c is the speed of light. The optical conductivity indicates the density of photo-excited electrons [52] and how much these electrons diffuse in the material [53]. The non-doped CuO thin film has a higher optical conductivity in the all-photon energy region in Fig. 5c. In these regions, more photo-excited charge carriers are formed in it compared
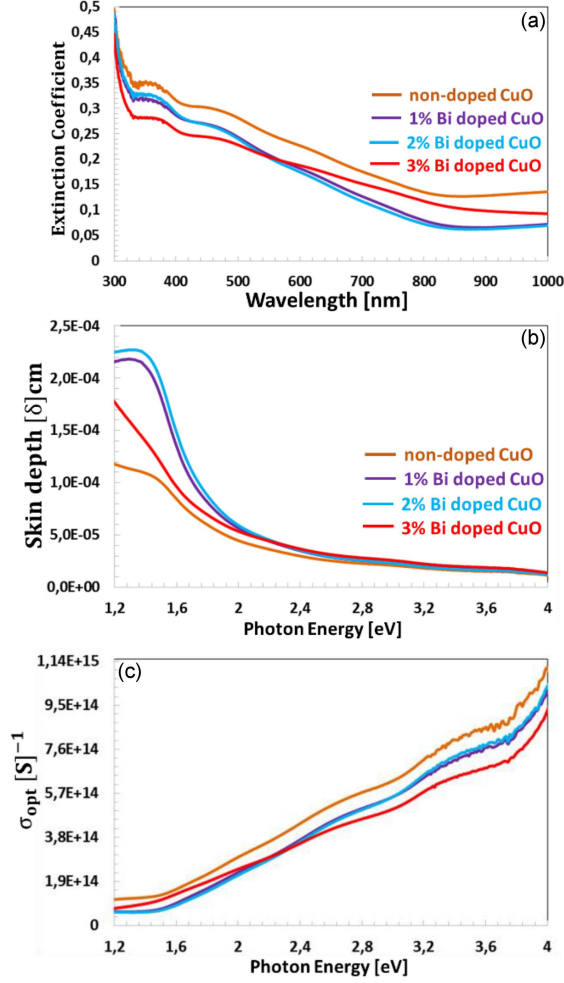
Fig. 5. (a) The extinction coefficient, (b) skin depth, and (c) optical conductivity of the non-doped and Bi-doped CuO samples.

to other thin films. For 2.4 eV and 4 eV energy ranges of the 1% and 2% Bi-doped CuO thin films, the photo-excited charge carriers formed in them increased more than once compared to those in Bi:CuO (3%) film.

3.4. Electrical characterization of non-doped and Bi:CuO/Si heterojunction

Considering the logarithmic (log.) characterization, $\log(J)$–$\log(V)$, of the non-doped and Bi-doped CuO/Si heterojunction photodetectors given in Fig. 6, the currents of these diodes are calculated [47] with the following

$$I = I_0 \left[\exp\left(\frac{qV}{nk_{\mathrm{B}}T} \right) - 1 \right], \qquad (13)$$

where V is the forward bias voltage applied, I_0 is the saturation current, k_{B} is the Boltzmann constant, n is the ideality factor, q is the electric charge, and T is the absolute temperature. The ideality factor of a heterojunction diode has been obtained by

$$n = \frac{q}{k_{\mathrm{B}}T} \frac{\mathrm{d}V}{\mathrm{d}(\ln(I))}, \qquad (14)$$

where I is the forward bias current. The ideality factor (n) has been obtained from the direct line drawn in the forward bias range of the $\log(J)$–$\log(V)$ curves in Fig. 6. According to the values given in Table III, the ideality factors of the photodetectors in the light are lower than in the darkness. In the illumination, the charge carriers formed by photo-excitation cause the current to increase and the ideality factor to remain low [48]. The ideality factors of 2% Bi-doped CuO/Si heterojunction diode for both environments are lower than the others. The better crystal structure of 2% Bi-doped CuO thin film and the larger crystal size limit the recombination of electron and hole charges. The lifetime of minority charge carriers is high in this thin film. In addition, a more intense charge transfer takes place in a thin film with a good crystalline structure. Therefore, they continue their way without much passivation in the recombination regions of photo-excited charge carriers, thus, the charge accumulation in the depletion region and the photocurrent increases. Thus, the J–V characteristic under illumination is different compared to other diodes. This indicates that the 2% Bi-doped CuO heterojunction diode has more ideal electrical properties.

The barrier height (Φ_b) of the diode is determined using

$$\Phi_b = \frac{k_{\mathrm{B}}T}{q} \ln\left(\frac{A\,A^*T^2}{I_0} \right), \qquad (15)$$

where A is the active area of the obtained diode and A^* is the effective Richardson constant ($\sim$ 112 A/cm^{2}K^2 for n-Si) [54] and I_0 was obtained directly from the point at which a line drawn intersects on y-axis of the reverse bias in the log J–V characteristic in Fig. 6. For all diodes, the barrier height in the light environment is lower than that in darkness. From this low barrier, the charge carriers formed are easier to transmit, and an increase in current can be achieved. In particular, the barrier height of 2% Bi-doped CuO heterojunction diode is lower, resulting in increased charge transfer and increased current.

TABLE III

The n (ideality factor) and Φ_b value of the non-doped and Bi-doped CuO/Si heterojunction photodetectors for the darkness and illumination.

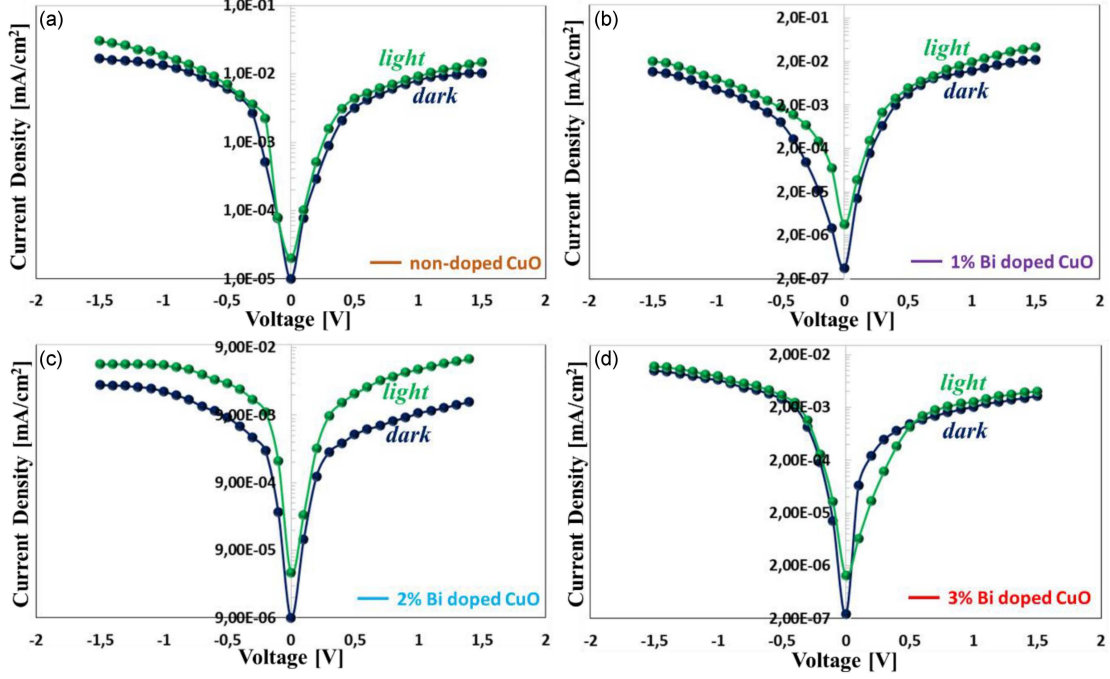| Sample	0% CuO:Bi	1% CuO:Bi	2% CuO:Bi	3% CuO:Bi
n (darkness)	2.86	2.65	1.78	3.01
n (light)	2.28	2.55	1.62	2.32
Φ_b (darkness)	0.63	0.70	0.61	0.65
Φ_b (light)	0.62	0.68	0.56	0.64

Fig. 6. The $\log(J)$–$\log(V)$ curves of (a) the non-doped, (b) 1%, (c) 2%, and (d) 3% Bi-doped CuO/Si heterojunction photodetectors.

The serial resistance (R_{serial}) [55] of heterojunction diodes can be analyzed by

$$R_{\text{serial}} = \frac{\Delta V_{\text{forward bias voltage}}}{\Delta I_{\text{forward bias current}}}. \qquad (16)$$

Serial resistances of heterojunction diodes have been analyzed by considering the ratio of the voltage difference to the current difference in the regions of forward and reverse bias [46], respectively, and are an important factor that influences the performance of photodetector. According to Fig. 7, the resistances of all the diodes were calculated to be more stable between 1.1 and 1.5 V. Serial resistances (R_s) values of non-doped, 1%, 2%, and 3% Bi-doped CuO/Si heterojunctions have been calculated by using (16) to be 0.083, 0.029, 0.013, and 0.348 Ω cm^2, respectively. Compared to other photodetectors, the resistance of 2% Bi-doped CuO photodetector was found to be lower because of a limited number of interface states and traps in 2% Bi-doped CuO thin film, its lower surface microstrain and dislocation density, more photo-excited charge transitions, and longer lifetime of minority charges. However, since Bi atoms occupy the interstitial sites in 3% Bi-doped CuO thin films, these sites act as recombination points, and the resistance of the heterojunction increases [48].

The photosensitivity (S) of the non-doped and Bi-doped CuO/Si heterojunction photodetectors under the incident light of 100 mW/cm^2 has been calculated by
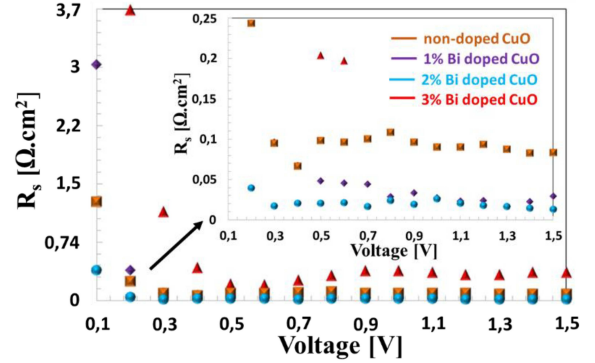
$$S = \frac{I_L - I_D}{I_D}, \qquad (17)$$

Fig. 7. Serial resistance (R_s) vs applied voltage curves of the non-doped and Bi-doped CuO/Si heterojunction photodetectors under the incident light of about 100 mW/cm^2.

where I_L is the photocurrent, I_D is the dark current. Among these photodetectors, the 2% Bi-doped CuO photodetector has exhibited the highest photosensitivity, as seen in Table IV. The electrical field may increase due to the doping effect in the depletion region of this heterojunction photodetector. This electric field enhances the separation of photo-excited charge carriers in the depletion region [56, 57], resulting in some increases in photosensitivity [58]. Furthermore, the high crystallinity of 2% Bi-doped CuO thin film leads to an increase in the lifetime of the photo-excited charge carriers and a higher photosensitivity. However, the poor crystal structure of 3% Bi-doped CuO thin film means

TABLE IV

The photosensitivity S, responsivity R, detectivity D, and the quantum efficiency of the non-doped and Bi-doped CuO/Si heterojunction photodetectors.

Samples	S	R [mA/W]	D ($\times 10^8$) [Jones]	Rise times	Fall times
Non-doped CuO	0.79	1.91	3.73	$\tau_{01} = 465$ ms	$\tau_{02} = 2.1$ s
1% Bi:CuO	0.68	1.15	3.57	$\tau_{11} = 882$ ms	$\tau_{12} = 2.61$ s
2% Bi:CuO	1.03	3.71	4.00	$\tau_{21} = 44$ ms	$\tau_{22} = 1.28$ s
3% Bi:CuO	0.20	0.28	2.51	$\tau_{31} = 1.92$ s	$\tau_{31} = 4.47$ s

that it may contain a large number of defects and traps [48]. Therefore, photo-excited charge carriers undergo recombination in these defects and traps, which decreases the lifetimes of these charge carriers and causes the photosensitivity to decrease.

The photocurrent per active area together with the light power is expressed as the responsivity (R) [59, 60, 61], i.e.,

$$R = \frac{I_L - I_D}{A\,P}, \tag{18}$$

where P is the light power [62]. According to data given in Table IV, 2% Bi-doped CuO photodetector has exhibited the highest responsivity, while 3% Bi-doped CuO photodetector has shown the lowest responsivity. The photo-excited charge carriers formed in the 2% Bi-doped CuO thin film with the advanced crystal structure diffuse to the depletion region without being excessively exposed to traps and defects, increasing the charge accumulation in the depletion region and the photocurrent, which in this case causes high responsivity [61]. The fact that the skin depth is high also confirms this situation. However, the photo-excited charge carriers formed in this thin film are subject to recombination within the defects and traps and undergo unwanted scattering from the grain boundaries due to the poor crystal structure. Thus, the charge transfer to the depletion region is limited, and the charge separation and photocurrent are reduced [58]. In addition, the crystal structure of the non-doped CuO thin film is very similar to that of Bi:CuO (2%) sample, and the crystallite size is large. This thin film absorbs more photons in UV and Vis regions compared to other samples. These factors increase photo-excited charge carriers in thin films and the charge aggregation in the depletion region and increase the photocurrent [60].

Another parameter that determines the performance of the photodetectors is the detectivity, which is expressed by (19) [60, 63]

$$D = \frac{R\sqrt{A}}{(2qI_D)^{1/2}}, \tag{19}$$

where q is the electronic charge [62, 64]. The detectivity indicates that very low signals are detected and measured. As seen in Table IV, the 2% Bi-doped CuO photodetector has shown the highest detectivity. This indicates that the noise current is low and the responsivity is high. However, the 3% Bi-doped CuO photodetector has a lower detectivity. The inability of the charge carriers in this thin film to diffuse to the depletion region properly, their scattering at the grain boundaries, and their random movement can cause noise in the device [58]. Therefore, a pronounced decrease in detectivity can occur.

The current density vs the time of the non-doped and Bi-doped CuO/Si heterojunction photodetectors under the sun light at 100 mW/cm^2 and a 5 V bias voltage is given in Fig. 8. The rise times and fall times of all photodetectors have been listed in Table IV. The rise times of these photodetectors have been determined to be from about 10% to 90% of the highest photocurrent density, while the fall times have been characterized as being from about 90% to 10% of the highest photocurrent density. According to data given in Table IV, the fact that the fall times of all photodetectors are longer than the rise times can be attributed to the trapping of the charge carriers in deep levels [59, 65]. The release of the charges trapped in the deep level of the band can be longer and, therefore, the fall time increases. Depending on the formation of photo-excited charge carriers in a thin film and its crystal structure, the diffusion of these charges must be very fast, but they are trapped by the defects [66, 67], limiting the time of rise and fall. While the rise and fall times of 2% Bi-doped CuO photodetector are shorter compared to other photodetectors, 3% Bi-doped CuO photodetector shows the longest rise and fall times. Electron–hole charges formed by photo-excitation in 2% Bi-doped CuO thin film with advanced crystal structure go to the depletion and contact regions quickly, without recombining in too many defects and traps, and lead to the response speed of the device. However, in the poor crystalline 3% Bi-doped CuO thin film, the charges undergo recombination by being exposed to the trap regions, and their travel to both regions is limited, causing the rise and fall times to increase [65]. In addition, I_{on}/I_{off} values of the non-doped, 1%, 2%, and 3% Bi-doped CuO photodetectors were 1.30, 1.12, 1.41, and 1.04, respectively [62]. Factors such as the lattice mismatch, parasitic generations, dangling bonds, and recombination points can cause the I_{on}/I_{off} rate to be small [65].
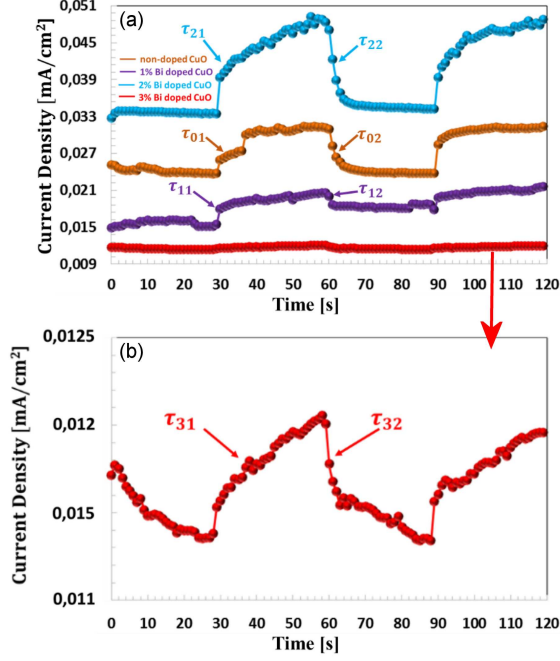
Fig. 8. The current density vs the time of the non-doped and Bi-doped CuO/Si heterojunction photodetectors under the sun light at 100 mW/cm².
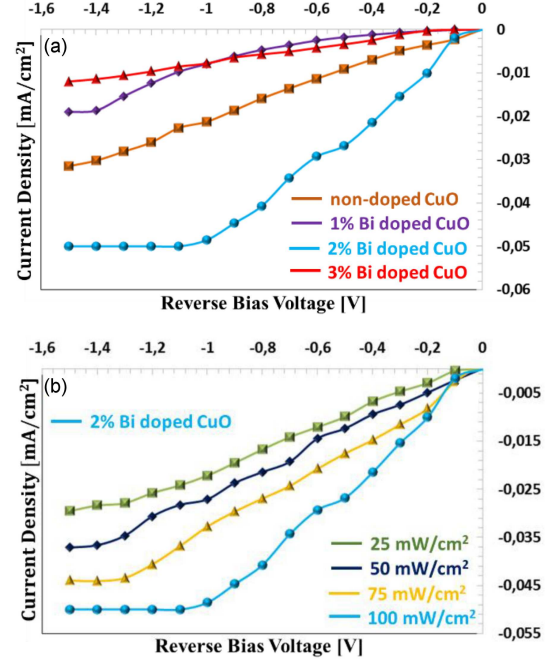

Fig. 9. (a) The current density vs reverse bias voltage characteristic of the non-doped and Bi:CuO/Si heterojunction photodetectors under the sun light at 100 mW/cm² power density. (b) The current density vs reverse bias voltage characteristic of 2% Bi:CuO/Si heterojunction photodetectors under the sun light at 25, 50, 75, and 100 mW/cm² power densities.

The current density vs reverse bias voltage characteristics of the non-doped and Bi-doped CuO/Si heterojunction photodetectors under the sun light at 100 mW/cm² are shown in Fig. 9a. According to the J–V characteristics (for reverse bias region) in Fig. 9a, the 2% Bi-doped CuO photodetector has shown the highest photocurrent. More electron–hole pairs were formed in the 2% Bi-doped CuO thin film. Minority charge carriers diffused more densely into the depletion region and increased charge accumulation in this region [58, 68, 69]. Thus, the width of the depletion region has increased, and the magnitude of the electrical field has increased in this region, resulting in higher charge separation [56, 57, 63]. Thus, the photocurrent increases even more in the reverse bias region. In addition, due to the coherent band alignment between the 2% Bi-doped CuO thin film and the Si semiconductors, an ideal charge transfer has occurred between the two semiconductors and contributed to the photocurrent. However, 3% Bi-doped CuO photodetector exhibited the lowest photocurrent. Interface states in the thin film, excess numbers of grain boundaries and defects and traps between these grain boundaries, dangling bonds between two semiconductors, and leakage current that limits the transfer of charge to the depletion region, negatively affect the electrical field and charge accumulation that will occur in the depletion region and cause the photocurrent to remain low. The photocurrent values of all photodetectors are compatible with their photosensitivity, responsivity, and detectivity according to the J–V characteristics in Fig. 9a.

The characteristics of J–V (for reverse bias range) of the 2% Bi-doped CuO photodetector under 25, 50, 75, and 100 mW/cm² power densities are shown in Fig. 9b [70]. The intensity of light penetration into the 2% Bi-doped CuO thin film increased as the sun's power density increased. The light has a high-power density that diffuses more into the depletion site and forms more photo-excited electron–hole pairs. As the number of charge carriers increases, accumulation of the charge in the depletion region increases, which results in a rise in the photocurrent [71–73]. Thus, the photodetector has shown the lowest photocurrent for 25 mW/cm² power density, while the highest photocurrent for 100 mW/cm² power density.

4. Conclusions

Non-doped and Bi-doped CuO thin films have been fabricated on SLG substrates by a spin coating technique with gradual annealing at 480°C for 1 h in air atmosphere. The effect of Bi doping on the crystal parameters and optical (absorbance and energy band gap), topological, and opto–electronic characterization of the samples was conducted using different measurement systems-based techniques. The obtained films had a tenorite polycrystalline nature with two main peaks around 35.9° and 39.0°,

with d_{hkl} of ~ 2.50 and 2.30 Å related to the (-111) and (200) planes, respectively. Crystal parameters of non-doped CuO film, including crystallite size, dislocation density, and micro-strain, changed with increasing Bi concentration.

It has been observed and determined that the thin film with the most homogeneous particle distribution is the Bi:CuO (2%) film. The optical properties of 2% and 1% thin films have been found to be close to each other and exhibited high photon transmission. The Bi:CuO (0%) film has high photon absorption. The refractive index of 2% Bi-doped CuO thin film is the lowest. The direct band gaps of the non-doped, 1%, 2%, and 3% Bi-doped CuO thin films were found to be 1.77, 1.89, 1.94, and 1.84 eV, respectively.

The ideality factor and barrier height of 2% Bi-doped CuO heterojunction for light and dark environments are lower than the others. Also, a 2% Bi-doped CuO thin film-based photodetector has higher photosensitivity, responsivity, and detectivity, and its rise and fall times are found to be lower. The crystal size of 2% Bi-doped CuO thin film for preferential orientation is large, and the crystal structure is the most developed. Therefore, traps and defects are limited in this thin film, and a large number of photo-excited charge carriers migrate rapidly and densely toward the depilation region. The wide depletion region and the high electric field magnitude cause charge separation in the depletion region and a high photocurrent. In addition, since 3% Bi-doped CuO thin film has the weakest crystal structure, electron and hole pairs are subject to recombination in a large number of defects and traps, compared to other thin films. In addition, the performance of 3% Bi-doped CuO thin-film heterojunction photodetector is very low due to the many interfacial states, leakage current, pendent bonds, and high series resistance.

References

[1] D.J. Lee, G.M. Kumar, Y. Kim, W.Yang, D.Y. Kim, T.W. Kang, P. Ilanchezhiyan, *J. Mater. Res. Technol.* **18** 4946 (2022).

[2] L. Shi, F Wang, B. Li, X. Chen, B. Yao, D. Zhao, D. Shen, *J. Mater. Chem.* **2**, 5005 (2014).

[3] J. Wang, S. Lee, *Sensors* **11**, 696 (2011).

[4] I.L.P. Raj, S. Valanarasu, A. Asuntha, R.S. Rimal Isaac, M. Shkir, H. Algarni, S. AlFaify, *J. Mater. Sci. Mater. Electron.* **33**, 11753 (2022).

[5] X. Zhao, G. Wang, H. Lin et al., *Nanomaterials* **11**, 1125 (2021).

[6] K. Mageshwari, R. Sathyamoorthy, *Mater. Sci. Semicond. Process.* **16**, 337 (2013).

[7] F.A. Akgul, G. Akgul, N. Yildirim, H.E. Unalan, R. Turan, *Mater. Chem. Phys.* **147**, 987 (2014).

[8] W.L. Yu, Y.Z. Lin, X.W. Zhu, Z.G. Hu, M.J. Han, S.S. Cai, L.L. Chen, H.H. Shao, *J. Appl. Phys.* **117**, 045701 (2015).

[9] S. Das, T.L. Alford, *J. Appl. Phys.* **113**, 244905 (2013).

[10] A. Bhaumik, A.M. Shearin, R. Patel, K. Ghosh, *Phys. Chem. Chem. Phys.* **16**, 11054 (2014).

[11] W. Shockley, H.J. Queisser, *J. Appl. Phys.* **32**, 510 (1961).

[12] T.KS. Wong, S. Zhuk, S. Masudy-Panah, G.K. Dalapati, *Materials* **9**, 271 (2016).

[13] D.P. Dubal, G.S. Gund, R. Holze, H.S. Jadhav, C.D. Lokhande, C.J. Park, *Dalton Trans.* **42**, 6459 (2013).

[14] K. Jindal, M. Tomar, V. Gupta, *Biosens. Bioelectron.* **38**, 11 (2012).

[15] B.E. Al-Jumaili, J.M. Rzaij, A.S. Ibra-heam, *Mater. Today Proc.* **42**, 2603 (2021).

[16] T. Ishihara, M. Higuchi, T. Takagi, M. Ito, H. Nishiguchi, Y. Takita, *J. Mater. Chem.* **8**, 2037 (1998).

[17] D. Naveena, R. Dhanabal, A.C. Bose, *Opt. Mater.* **127**, 112266 (2022).

[18] Z. Zang, A. Nakamura, J. Temmyo, *Mater. Lett.* **92**, 188 (2013).

[19] W. Peng, Y. Zhou, J. Li et al., *Mater. Sci. Semicond. Process.* **131**, 105883 (2021).

[20] Q. Pan, H. Jin, H. Wang, G. Yin, *Electrochimica Acta* **53**, 951 (2007).

[21] F.E. Oropeza, N.Y. Dzade, A. Pons-Martí, Z. Yang, K.H.L. Zhang, N.H. De Leeuw, P. Hofmann, *J. Phys. Chem.* **124**, 22416 (2020).

[22] D.J. Payne, M.D.M. Robinson, R.G. Egdell, A. Walsh, J. McNulty, K.E. Smith, L.F.J. Piper, *Appl. Phys. Lett.* **98**, 212110 (2011).

[23] J. Shi, E.A. Rubinstein, W. Li et al., *Adv. Sci.* **9**, 2104141 (2022).

[24] D. Puzikova, M. Dergacheva, G. Khussurova, in: *7th Int. Conf. on Nanomaterials and Advanced Energy Storage Systems (INESS-2020)*, 2020.

[25] H. Gao, F. Wang, S. Wang, X. Wang, Z. Yi, H. Yang, *Mater. Res. Bull.* **115**, 140 (2019).

[26] D. Roy, G.F. Samu, M.K. Hossain, C. Janáky, K. Rajeshwar, *Catal. Today* **300**, 136 (2018).

[27] J. Zheng, W. Zhang, Z. Lin, C. Wei, W. Yang, P. Dong, S. Hu, *J. Mater. Chem. B* **4**, 1247 (2016).

[28] M. Izaki, Y. Yamane, J. Sasano, T. Shinagawa, M. Inoue, *Electrochem. Solid-State Lett.* **14**, 30 (2010).

[29] F. Janene, H. Dhaouadi, L. Arfaoui, N. Etteyeb, F. Touati, *Ionics* **22**, 1395 (2016).

[30] R.R. Prabhu, A.C. Saritha, M.R. Shijeesh, M.K. Jayaraj, *Mater. Sci. Eng. B* **220**, 82 (2017).

[31] S. Annathurai, S. Chidambaram, B. Baskaran, G.K.D. Prasanna Venkatesan, *J. Inorg. Organomet. Polym. Mater.* **29**, 535 (2019).

[32] K. Zhang, M. Peng, W. Wu et al., *Mater. Horiz.* **4**, 274 (2017).

[33] Q. Hong, Y. Cao, J. Xu, H. Lu, J. He, J.L. Sun, *ACS Appl. Mater. Interfaces* **6**, 20887 (2014).

[34] Q.M. Fu, D.C. He, Z.C. Yao et al., *Mater. Lett.* **222**, 74 (2018).

[35] E. Aydin, M. Sankir, N.D. Sankir, *J. Alloys Compd.* **603**, 119 (2014).

[36] H.S.H. Mohamed, M. Abdel-Hafiez, B.N. Miroshnikov, A.D. Barinov, I.N. Miroshnikova, *Mater. Sci. Semicond. Process.* **27**, 725 (2014).

[37] M. Kölbach, H. Hempel, K. Harbauer et al., *ACS Appl. Energy Mater.* **3**, 4320 (2020).

[38] M.J. Hong, Y.C. Lin, L.C. Chao, P.H. Lin, B.R. Huang, *Appl. Surf. Sci.* **346**, 18 (2015).

[39] R. Sun, J. Guo, C. Sun, et al, *Energy Environ. Sci.* **12**, 384 (2019).

[40] D. Thangaraju, R. Marnadu, V. Santhana, A. Durairajan, P. Kathirvel, J. Chandrasekaran, M.A. Valente, D.C. Greenidge, *CrystEngComm.* **22**, 525 (2020).

[41] M.R. Johan, M.S.M. Suan, N.L. Hawari, H.A. Ching, *Int. J. Electrochem. Sci.* **6**, 6094 (2011).

[42] U. Holzwarth, N. Gibson, *Nat. Nanotechnol.* **6**, 534 (2011).

[43] H.A.S. Qutbi, A.M. Saleh, M.O. Dawood, N. Habubi, S.S. Chiad, *Int. J. Mech. Eng.* **7**, 2030 (2022).

[44] R.K. Gupta, K. Ghosh, R. Patel, S.R. Mishra, P.K. Kahol, *Mater. Lett.* **62**, 3373 (2008).

[45] G. Ramanathan, R.J. Xavier, K.R. Murali, *Elixir Thin Film Technol.* **50**, 10588 (2012).

[46] T.S. Moss, *Phys. Status Solidi (b)* **131**, 415 (1985).

[47] P.J.L. Herve, L.K.J. Vandamme, *J. Appl. Phys.* **77**, 5476 (1995).

[48] R.A. Ismail, A.M. Mousa, S.S. Shaker, *Opt. Quantum Electron.* **51**, 1 (2019).

[49] N.M. Ravindra, P. Ganapathy, J. Choi, *Infrared Phys. Technol.* **50**, 21 (2007).

[50] M.S. Al Khalifah, I.M. El Radaf, M.S. El-Bana, *J. Alloys Compd.* **813**, 152169 (2020).

[51] M.I. Fathima, A.M.S. Arulanantham, K.J. Wilson, *Mater. Res. Express* **7**, 015510 (2020).

[52] I.M. El Radaf, *J. Mater. Sci. Mater. Electron.* **31**, 3228 (2020).

[53] A. Ziti, B. Hartiti, H. Labrim, S. Fadili, H.J. Tchognia Nkuissi, A. Ridah, P. Thevenin, *Appl. Phys. A* **125**, 1 (2019).

[54] Ö. Güllü, S. Asubay, Ş. Aydoğan, A. Türüt, *Phys. E: Low-Dimens. Syst. Nanostruct.* **42**, 1411 (2010).

[55] H.S. Soliman, A.A.M. Farag, N.M. Khosifan, T.S. Solami, *J. Alloys Compd.* **530**, 157 (2012).

[56] H.K. Hassun, B.H. Hussein, E.M. Salman, A.H. Shaban, *Energy Rep.* **6**, 46 (2020).

[57] N. Jhansi, D. Balasubramanian, J.H. Chang, K. Mohanraj, R. Marnadu, M.A. Manthrammel, M. Shkir, *Silicon* **1**11 (2022).

[58] H.T. Hussein, M.K. Mohammed, R.I. Kamel, U.M. Nayef, *Chem. Pap.* **75**, 6257 (2021).

[59] I.L.P. Raj, N. Chidhambaram, S. Saravanakumar, S. Sasikumar, S. Varadharajaperumal, D. Alagarasan, T. Alshahrani, M. Shkir, *Optik* **241**, 166406 (2021).

[60] S.K. Kajli, D. Ray, S.C. Roy, *J. Alloys Compd.* **895**, 162546 (2022).

[61] R.A. Ismail, N.F. Habubi, E.H. Hadi, *Optik* **147**, 391 (2017).

[62] S. Raveesh, V.K.S. Yadav, R. Paily, *IEEE Electron Device Lett.* **42**, 1021 (2021).

[63] R.A. Ismail, A.D. Faisal, S.S. Shaker, *Opt. Mater.* **133**, 112998 (2022).

[64] Z. Wang, X. Zhang, D. Wu, J. Guo, Z. Zhao, Z. Shi, Y. Tian, X. Huang, X. Li, *J. Mater. Chem.* **8**, 6877 (2020).

[65] H.S. Kim, M.D. Kumar, M. Patel, J. Kim, *Sens. Actuators Phys.* **252**, 35 (2016).

[66] M.A. Basyooni, W. Belaid, A. Houimi, S.E. Zaki, Y.R. Eker, S. Yiğit Gezgin, H.Ş. Kiliç, *Opt. Mater.* **128**, 112389 (2022).

[67] F. Aslan, H. Esen, F. Yakuphanoglu, *Silicon* **12**, 2149 (2020).

[68] A.D. Nusseif, A.M. Abdul-Majeed, N.S. Hameed, *Silicon* **14**, 1817 (2022).

[69] A. Kompa, D. Kekuda, M.S. Murari, *Opt. Mater.* **126**, 112212 (2022).

[70] M.H. Mohsin, R.A. Ismail, R.O. Mhadi, *Appl. Phys. A* **127**, 214 (2021).

[71] L. Shi, F. Wang, B. Li, X. Chen, B. Yao, D. Zhao, D. Shen, *J. Mater. Chem.* **2**, 5005 (2014).

[72] B.A.H. Ameen, A. Yildiz, W.A Farooq, F. Yakuphanoglu, *Silicon* **11**, 563 (2019).

[73] R.A. Ismail, A.M. Mousa, Z.T. Hussain, *Optik* **139**, 328 (2017).